Search for new heavy particles decaying to $ZZ \to llll$, $lljj$ in $p\bar{p}$ collisions at $\sqrt{s} = 1.96$ TeV

T. Aaltonen,[21] B. Álvarez González,[9,w] S. Amerio,[41a] D. Amidei,[32] A. Anastassov,[36] A. Annovi,[17] J. Antos,[12]
G. Apollinari,[15] J. A. Appel,[15] A. Apresyan,[46] T. Arisawa,[56] A. Artikov,[13] J. Asaadi,[51] W. Ashmanskas,[15] B. Auerbach,[59]
A. Aurisano,[51] F. Azfar,[40] W. Badgett,[15] A. Barbaro-Galtieri,[26] V. E. Barnes,[46] B. A. Barnett,[23] P. Barria,[44c,44a] P. Bartos,[12]
M. Bauce,[41b,41a] G. Bauer,[30] F. Bedeschi,[44a] D. Beecher,[28] S. Behari,[23] G. Bellettini,[44b,44a] J. Bellinger,[58] D. Benjamin,[14]
A. Beretvas,[15] A. Bhatti,[48] M. Binkley,[15,a] D. Bisello,[41b,41a] I. Bizjak,[28,aa] K. R. Bland,[5] B. Blumenfeld,[23] A. Bocci,[14]
A. Bodek,[47] D. Bortoletto,[46] J. Boudreau,[45] A. Boveia,[11] B. Brau,[15,b] L. Brigliadori,[6b,6a] A. Brisuda,[12] C. Bromberg,[33]
E. Brucken,[21] M. Bucciantonio,[44b,44a] J. Budagov,[13] H. S. Budd,[47] S. Budd,[22] K. Burkett,[15] G. Busetto,[41b,41a] P. Bussey,[19]
A. Buzatu,[31] C. Calancha,[29] S. Camarda,[4] M. Campanelli,[33] M. Campbell,[32] F. Canelli,[12,15] A. Canepa,[43] B. Carls,[22]
D. Carlsmith,[58] R. Carosi,[44a] S. Carrillo,[16,l] S. Carron,[15] B. Casal,[9] M. Casarsa,[15] A. Castro,[6b,6a] P. Catastini,[15] D. Cauz,[52a]
V. Cavaliere,[44c,44a] M. Cavalli-Sforza,[4] A. Cerri,[26,g] L. Cerrito,[28,r] Y. C. Chen,[1] M. Chertok,[a7] G. Chiarelli,[44a]
G. Chlachidze,[15] F. Chlebana,[15] K. Cho,[25] D. Chokheli,[13] J. P. Chou,[20] W. H. Chung,[58] Y. S. Chung,[47] C. I. Ciobanu,[42]
M. A. Ciocci,[44c,44a] A. Clark,[18] G. Compostella,[41b,41a] M. E. Convery,[15] J. Conway,[a7] M. Corbo,[42] M. Cordelli,[17]
C. A. Cox,[a7] D. J. Cox,[a7] F. Crescioli,[44b,44a] C. Cuenca Almenar,[59] J. Cuevas,[9,w] R. Culbertson,[15] D. Dagenhart,[15]
N. d'Ascenzo,[42,u] M. Datta,[15] P. de Barbaro,[47] S. De Cecco,[49a] G. De Lorenzo,[4] M. Dell'Orso,[44b,44a] C. Deluca,[4]
L. Demortier,[48] J. Deng,[14,d] M. Deninno,[6a] F. Devoto,[21] M. d'Errico,[41b,41a] A. Di Canto,[44b,44a] B. Di Ruzza,[44a]
J. R. Dittmann,[5] M. D'Onofrio,[27] S. Donati,[44b,44a] P. Dong,[15] M. Dorigo,[52a] T. Dorigo,[41a] K. Ebina,[56] A. Elagin,[51]
A. Eppig,[32] R. Erbacher,[a7] D. Errede,[22] S. Errede,[22] N. Ershaidat,[42,z] R. Eusebi,[51] H. C. Fang,[26] S. Farrington,[40]
M. Feindt,[24] J. P. Fernandez,[29] C. Ferrazza,[44d,44a] R. Field,[16] G. Flanagan,[46,s] R. Forrest,[a7] M. J. Frank,[5] M. Franklin,[20]
J. C. Freeman,[15] Y. Funakoshi,[56] I. Furic,[16] M. Gallinaro,[48] J. Galyardt,[10] J. E. Garcia,[18] A. F. Garfinkel,[46] P. Garosi,[44c,44a]
H. Gerberich,[22] E. Gerchtein,[15] S. Giagu,[49b,49a] V. Giakoumopoulou,[3] P. Giannetti,[44a] K. Gibson,[45] C. M. Ginsburg,[15]
N. Giokaris,[3] P. Giromini,[17] M. Giunta,[44a] G. Giurgiu,[23] V. Glagolev,[13] D. Glenzinski,[15] M. Gold,[35] D. Goldin,[51]
N. Goldschmidt,[16] A. Golossanov,[15] G. Gomez,[9] G. Gomez-Ceballos,[30] M. Goncharov,[30] O. González,[29] I. Gorelov,[35]
A. T. Goshaw,[14] K. Goulianos,[48] A. Gresele,[41a] S. Grinstein,[4] C. Grosso-Pilcher,[11] R. C. Group,[55] J. Guimaraes da Costa,[20]
Z. Gunay-Unalan,[33] C. Haber,[26] S. R. Hahn,[15] E. Halkiadakis,[50] A. Hamaguchi,[39] J. Y. Han,[47] F. Happacher,[17] K. Hara,[53]
D. Hare,[50] M. Hare,[54] R. F. Harr,[57] K. Hatakeyama,[5] C. Hays,[40] M. Heck,[24] J. Heinrich,[43] M. Herndon,[58] S. Hewamanage,[5]
D. Hidas,[50] A. Hocker,[15] W. Hopkins,[15,h] D. Horn,[24] S. Hou,[1] R. E. Hughes,[37] M. Hurwitz,[11] U. Husemann,[59] N. Hussain,[31]
M. Hussein,[33] J. Huston,[33] G. Introzzi,[44a] M. Iori,[49b,49a] A. Ivanov,[a7,p] E. James,[15] D. Jang,[10] B. Jayatilaka,[14] E. J. Jeon,[25]
M. K. Jha,[6a] S. Jindariani,[15] W. Johnson,[a7] M. Jones,[46] K. K. Joo,[25] S. Y. Jun,[10] T. R. Junk,[15] T. Kamon,[51] P. E. Karchin,[57]
Y. Kato,[39,o] W. Ketchum,[11] J. Keung,[43] V. Khotilovich,[51] B. Kilminster,[15] D. H. Kim,[25] H. S. Kim,[25] H. W. Kim,[25]
J. E. Kim,[25] M. J. Kim,[17] S. B. Kim,[25] S. H. Kim,[53] Y. K. Kim,[11] N. Kimura,[56] M. Kirby,[15] S. Klimenko,[16] K. Kondo,[56]
D. J. Kong,[25] J. Konigsberg,[16] A. V. Kotwal,[14] M. Kreps,[24] J. Kroll,[43] D. Krop,[11] N. Krumnack,[5,m] M. Kruse,[14]
V. Krutelyov,[51,e] T. Kuhr,[24] M. Kurata,[53] S. Kwang,[11] A. T. Laasanen,[46] S. Lami,[44a] S. Lammel,[15] M. Lancaster,[28]
R. L. Lander,[a7] K. Lannon,[37,v] A. Lath,[50] G. Latino,[44c,44a] I. Lazzizzera,[41a] T. LeCompte,[2] E. Lee,[51] H. S. Lee,[11] J. S. Lee,[25]
S. W. Lee,[51,x] S. Leo,[44b,44a] S. Leone,[44a] J. D. Lewis,[15] C.-J. Lin,[26] J. Linacre,[40] M. Lindgren,[15] E. Lipeles,[43] A. Lister,[18]
D. O. Litvintsev,[15] C. Liu,[45] Q. Liu,[46] T. Liu,[15] S. Lockwitz,[59] N. S. Lockyer,[43] A. Loginov,[59] D. Lucchesi,[41b,41a]
J. Lueck,[24] P. Lujan,[26] P. Lukens,[15] G. Lungu,[48] J. Lys,[26] R. Lysak,[12] R. Madrak,[15] K. Maeshima,[15] K. Makhoul,[30]
P. Maksimovic,[23] S. Malik,[48] G. Manca,[27,c] A. Manousakis-Katsikakis,[3] F. Margaroli,[46] C. Marino,[24] M. Martínez,[4]
R. Martínez-Ballarín,[29] P. Mastrandrea,[49a] M. Mathis,[23] M. E. Mattson,[57] P. Mazzanti,[6a] K. S. McFarland,[47] P. McIntyre,[51]
R. McNulty,[27,j] A. Mehta,[27] P. Mehtala,[21] A. Menzione,[44a] C. Mesropian,[48] T. Miao,[15] D. Mietlicki,[32] A. Mitra,[1]
H. Miyake,[53] S. Moed,[20] N. Moggi,[6a] M. N. Mondragon,[15,l] C. S. Moon,[25] R. Moore,[15] M. J. Morello,[15] J. Morlock,[24]
P. Movilla Fernandez,[15] A. Mukherjee,[15] Th. Muller,[24] P. Murat,[15] M. Mussini,[6b,6a] J. Nachtman,[15,n] Y. Nagai,[53]
J. Naganoma,[56] I. Nakano,[38] A. Napier,[54] J. Nett,[51] C. Neu,[55] M. S. Neubauer,[22] J. Nielsen,[26,f] L. Nodulman,[2]
O. Norniella,[22] E. Nurse,[28] L. Oakes,[40] S. H. Oh,[14] Y. D. Oh,[25] I. Oksuzian,[55] T. Okusawa,[39] R. Orava,[21] L. Ortolan,[4]
S. Pagan Griso,[41b,41a] C. Pagliarone,[52a] E. Palencia,[9,g] V. Papadimitriou,[15] A. A. Paramonov,[2] J. Patrick,[15]
G. Pauletta,[52b,52a] M. Paulini,[10] C. Paus,[30] D. E. Pellett,[a7] T. J. Phillips,[14] G. Piacentino,[44a] E. Pianori,[43]
J. Pilot,[37] K. Pitts,[22] C. Plager,[8] L. Pondrom,[58] K. Potamianos,[46] O. Poukhov,[13,a] F. Prokoshin,[13,y] A. Pronko,[15]
F. Ptohos,[17,i] E. Pueschel,[10] G. Punzi,[44b,44a] J. Pursley,[58] A. Rahaman,[45] V. Ramakrishnan,[58] N. Ranjan,[46] I. Redondo,[29]
P. Renton,[40] M. Rescigno,[49a] F. Rimondi,[6b,6a] L. Ristori,[45,15] A. Robson,[19] T. Rodrigo,[9] T. Rodriguez,[43] E. Rogers,[22]
S. Rolli,[54] R. Roser,[15] M. Rossi,[52a] F. Rubbo,[15] F. Ruffini,[44c,44a] A. Ruiz,[9] J. Russ,[10] V. Rusu,[15] A. Safonov,[51]

W. K. Sakumoto,[47] Y. Sakurai,[56] L. Santi,[52b,52a] L. Sartori,[44a] K. Sato,[53] V. Saveliev,[42,u] A. Savoy-Navarro,[42] P. Schlabach,[15] A. Schmidt,[24] E. E. Schmidt,[15] M. P. Schmidt,[59,a] M. Schmitt,[36] T. Schwarz,[a7] L. Scodellaro,[9] A. Scribano,[44c,44a] F. Scuri,[44a] A. Sedov,[46] S. Seidel,[35] Y. Seiya,[39] A. Semenov,[13] F. Sforza,[44b,44a] A. Sfyrla,[22] S. Z. Shalhout,[a7] T. Shears,[27] P. F. Shepard,[45] M. Shimojima,[53,t] S. Shiraishi,[11] M. Shochet,[11] I. Shreyber,[34] A. Simonenko,[13] P. Sinervo,[31] A. Sissakian,[13,a] K. Sliwa,[54] J. R. Smith,[a7] F. D. Snider,[15] A. Soha,[15] S. Somalwar,[50] V. Sorin,[4] P. Squillacioti,[15] M. Stancari,[15] M. Stanitzki,[59] R. St. Denis,[19] B. Stelzer,[31] O. Stelzer-Chilton,[31] D. Stentz,[36] J. Strologas,[35] G. L. Strycker,[32] D. Stuart,[15,e] Y. Sudo,[53] A. Sukhanov,[16] I. Suslov,[13] K. Takemasa,[53] Y. Takeuchi,[53] J. Tang,[11] M. Tecchio,[32] P. K. Teng,[1] J. Thom,[15,h] J. Thome,[10] G. A. Thompson,[22] E. Thomson,[43] P. Ttito-Guzmán,[29] S. Tkaczyk,[15] D. Toback,[51] S. Tokar,[12] K. Tollefson,[33] T. Tomura,[53] D. Tonelli,[15] S. Torre,[17] D. Torretta,[15] P. Totaro,[52b,52a] M. Trovato,[44d,44a] Y. Tu,[43] F. Ukegawa,[53] S. Uozumi,[25] A. Varganov,[32] F. Vázquez,[16,l] G. Velev,[15] C. Vellidis,[3] M. Vidal,[29] I. Vila,[9] R. Vilar,[9] J. Vizán,[9] M. Vogel,[35] G. Volpi,[44b,44a] P. Wagner,[43] R. L. Wagner,[15] T. Wakisaka,[39] R. Wallny,[8] S. M. Wang,[1] A. Warburton,[31] D. Waters,[28] M. Weinberger,[51] W. C. Wester III,[15] B. Whitehouse,[54] D. Whiteson,[43,d] A. B. Wicklund,[2] E. Wicklund,[15] S. Wilbur,[11] F. Wick,[24] H. H. Williams,[43] J. S. Wilson,[37] P. Wilson,[15] B. L. Winer,[37] P. Wittich,[15,h] S. Wolbers,[15] H. Wolfe,[37] T. Wright,[32] X. Wu,[18] Z. Wu,[5] K. Yamamoto,[39] J. Yamaoka,[14] T. Yang,[15] U. K. Yang,[11,q] Y. C. Yang,[25] W.-M. Yao,[26] G. P. Yeh,[15] K. Yi,[15,n] J. Yoh,[15] K. Yorita,[56] T. Yoshida,[39,k] G. B. Yu,[14] I. Yu,[25] S. S. Yu,[15] J. C. Yun,[15] A. Zanetti,[52a] Y. Zeng,[14] and S. Zucchelli[6b,6b]

(CDF Collaboration)

[1]*Institute of Physics, Academia Sinica, Taipei, Taiwan 11529, Republic of China*
[2]*Argonne National Laboratory, Argonne, Illinois 60439, USA*
[3]*University of Athens, 157 71 Athens, Greece*
[4]*Institut de Fisica d'Altes Energies, ICREA, Universitat Autonoma de Barcelona, E-08193,
Bellaterra (Barcelona), Spain*
[5]*Baylor University, Waco, Texas 76798, USA*
[6a]*Istituto Nazionale di Fisica Nucleare Bologna, I-40127 Bologna, Italy*
[6b]*University of Bologna, I-40127 Bologna, Italy*
[a7]*University of California, Davis, Davis, California 95616, USA*
[8]*University of California, Los Angeles, Los Angeles, California 90024, USA*
[9]*Instituto de Fisica de Cantabria, CSIC-University of Cantabria, 39005 Santander, Spain*
[10]*Carnegie Mellon University, Pittsburgh, Pennsylvania 15213, USA*
[11]*Enrico Fermi Institute, University of Chicago, Chicago, Illinois 60637, USA*
[12]*Comenius University, 842 48 Bratislava, Slovakia; Institute of Experimental Physics, 040 01 Kosice, Slovakia*
[13]*Joint Institute for Nuclear Research, RU-141980 Dubna, Russia*
[14]*Duke University, Durham, North Carolina 27708, USA*
[15]*Fermi National Accelerator Laboratory, Batavia, Illinois 60510, USA*
[16]*University of Florida, Gainesville, Florida 32611, USA*
[17]*Laboratori Nazionali di Frascati, Istituto Nazionale di Fisica Nucleare, I-00044 Frascati, Italy*
[18]*University of Geneva, CH-1211 Geneva 4, Switzerland*
[19]*Glasgow University, Glasgow G12 8QQ, United Kingdom*
[20]*Harvard University, Cambridge, Massachusetts 02138, USA*
[21]*Division of High Energy Physics, Department of Physics, University of Helsinki and Helsinki Institute of Physics,
FIN-00014, Helsinki, Finland*
[22]*University of Illinois, Urbana, Illinois 61801, USA*
[23]*The Johns Hopkins University, Baltimore, Maryland 21218, USA*
[24]*Institut für Experimentelle Kernphysik, Karlsruhe Institute of Technology,
D-76131 Karlsruhe, Germany*
[25]*Center for High Energy Physics: Kyungpook National University, Daegu 702-701, Korea,
Seoul National University, Seoul 151-742, Korea; Sungkyunkwan University, Suwon 440-746,
Korea; Korea Institute of Science and Technology Information, Daejeon 305-806,
Korea; Chonnam National University, Gwangju 500-757, Korea; Chonbuk National University,
Jeonju 561-756, Korea*
[26]*Ernest Orlando Lawrence Berkeley National Laboratory, Berkeley, California 94720, USA*
[27]*University of Liverpool, Liverpool L69 7ZE, United Kingdom*
[28]*University College London, London WC1E 6BT, United Kingdom*
[29]*Centro de Investigaciones Energeticas Medioambientales y Tecnologicas, E-28040 Madrid, Spain*
[30]*Massachusetts Institute of Technology, Cambridge, Massachusetts 02139, USA*

[31]*Institute of Particle Physics: McGill University, Montréal, Québec, Canada H3A 2T8; Simon Fraser University, Burnaby, British Columbia, Canada V5A 1S6; University of Toronto, Toronto, Ontario, Canada M5S 1A7; and TRIUMF, Vancouver, British Columbia, Canada V6T 2A3*

[32]*University of Michigan, Ann Arbor, Michigan 48109, USA*

[33]*Michigan State University, East Lansing, Michigan 48824, USA*

[34]*Institution for Theoretical and Experimental Physics, ITEP, Moscow 117259, Russia*

[35]*University of New Mexico, Albuquerque, New Mexico 87131, USA*

[36]*Northwestern University, Evanston, Illinois 60208, USA*

[37]*The Ohio State University, Columbus, Ohio 43210, USA*

[38]*Okayama University, Okayama 700-8530, Japan*

[39]*Osaka City University, Osaka 588, Japan*

[40]*University of Oxford, Oxford OX1 3RH, United Kingdom*

[41a]*Istituto Nazionale di Fisica Nucleare, Sezione di Padova-Trento, I-35131 Padova, Italy*

[41b]*University of Padova, I-35131 Padova, Italy*

[42]*LPNHE, Universite Pierre et Marie Curie/IN2P3-CNRS, UMR7585, Paris, F-75252 France*

[43]*University of Pennsylvania, Philadelphia, Pennsylvania 19104, USA*

[44a]*Istituto Nazionale di Fisica Nucleare Pisa, I-56127 Pisa, Italy*

[44b]*University of Pisa, I-56127 Pisa, Italy*

[44c]*University of Siena, I-56127 Pisa, Italy*

[44d]*Scuola Normale Superiore, I-56127 Pisa, Italy*

[45]*University of Pittsburgh, Pittsburgh, Pennsylvania 15260, USA*

[46]*Purdue University, West Lafayette, Indiana 47907, USA*

[47]*University of Rochester, Rochester, New York 14627, USA*

[48]*The Rockefeller University, New York, New York 10065, USA*

[49a]*Istituto Nazionale di Fisica Nucleare, Sezione di Roma 1, I-00185 Roma, Italy*

[49b]*Sapienza Università di Roma, I-00185 Roma, Italy*

[50]*Rutgers University, Piscataway, New Jersey 08855, USA*

[51]*Texas A&M University, College Station, Texas 77843, USA*

[52a]*Istituto Nazionale di Fisica Nucleare Trieste/Udine, I-34100 Trieste, I-33100 Udine, Italy*

[52b]*University of Trieste/Udine, I-33100 Udine, Italy*

[53]*University of Tsukuba, Tsukuba, Ibaraki 305, Japan*

[54]*Tufts University, Medford, Massachusetts 02155, USA*

[a]Deceased

[b]With visitor from University of Massachusetts Amherst, Amherst, MA 01003, USA

[c]With visitor from Istituto Nazionale di Fisica Nucleare, Sezione di Cagliari, 09042 Monserrato (Cagliari), Italy.

[d]With visitor from University of California Irvine, Irvine, CA 92697, USA

[e]With visitor from University of California Santa Barbara, Santa Barbara, CA 93106, USA

[f]With visitor from University of California Santa Cruz, Santa Cruz, CA 95064, USA

[g]With visitor from CERN,CH-1211 Geneva, Switzerland

[h]With visitor from Cornell University, Ithaca, NY 14853, USA

[i]With visitor from University of Cyprus, Nicosia CY-1678, Cyprus

[j]With visitor from University College Dublin, Dublin 4, Ireland

[k]With visitor from University of Fukui, Fukui City, Fukui Prefecture, Japan 910-0017

[l]With visitor from Universidad Iberoamericana, Mexico D. F., Mexico

[m]With visitor from Iowa State University, Ames, IA 50011, USA

[n]With visitor from University of Iowa, Iowa City, IA 52242, USA

[o]With visitor from Kinki University, Higashi-Osaka City, Japan 577-8502

[p]With visitor from Kansas State University, Manhattan, KS 66506, USA

[q]With visitor from University of Manchester, Manchester M13 9PL, England

[r]With visitor from Queen Mary, University of London, London, E1 4NS, England

[s]With visitor from Muons, Inc., Batavia, IL 60510, USA

[t]With visitor from Nagasaki Institute of Applied Science, Nagasaki, Japan

[u]With visitor from National Research Nuclear University, Moscow, Russia

[v]With visitor from University of Notre Dame, Notre Dame, IN 46556, USA

[w]With visitor from Universidad de Oviedo, E-33007 Oviedo, Spain

[x]With visitor from Texas Tech University, Lubbock, TX 79609, USA

[y]With visitor from Universidad Tecnica Federico Santa Maria, 110v Valparaiso, Chile

[z]With visitor from Yarmouk University, Irbid 211-63, Jordan

[aa]On leave from J. Stefan Institute, Ljubljana, Slovenia

^{55}*University of Virginia, Charlottesville, Virginia 22906, USA*
^{56}*Waseda University, Tokyo 169, Japan*
^{57}*Wayne State University, Detroit, Michigan 48201, USA*
^{58}*University of Wisconsin, Madison, Wisconsin 53706, USA*
^{59}*Yale University, New Haven, Connecticut 06520, USA*

We report on a search for anomalous production of Z boson pairs through a massive resonance decay in data corresponding to 2.5–2.9 fb^{-1} of integrated luminosity in $p\bar{p}$ collisions at $\sqrt{s} = 1.96$ TeV using the CDF II detector at the Fermilab Tevatron. This analysis, with more data and channels where the Z bosons decay to muons or jets, supersedes the 1.1 fb^{-1} four-electron channel result previously published by CDF. In order to maintain high efficiency for muons, we use a new forward tracking algorithm and muon identification requirements optimized for these high signal-to-background channels. Predicting the dominant backgrounds in each channel entirely from sideband data samples, we observe four-body invariant mass spectra above 300 GeV/c^2 that are consistent with background. We set limits using the acceptance for a massive graviton resonance that are 7–20 times stronger than the previously published direct limits on resonant ZZ diboson production.

I. INTRODUCTION

The standard model of particle physics (SM) has been enormously successful, but many key questions remain to be answered by a more complete theory. New theoretical ideas can be tested with collider experiments, but it is also worthwhile for experiments to search broadly for anomalous "signatures." One common tactic is to look where experiments are keenly sensitive. The consummate example of this method is the Z' boson search, in which a low-background, well-understood observable (the dilepton invariant mass) is used to constrain the new physics models that predict a dilepton resonance. Diboson resonance searches are an attractive analog of the Z' boson searches, involving higher multiplicities of the same outgoing particles and additional mass constraints, both of which serve to further suppress experimental backgrounds. Dibosons are the dominant channels for high mass Higgs searches, and new physics scenarios predict particles such as Randall-Sundrum gravitons which would decay into dibosons [1]. The irreducible SM diboson background processes occur at such a low rate that they have only recently been observed at the Tevatron [2,3] at low diboson mass ($M_{ZZ} < 300$ GeV/c^2). At high diboson mass ($M_{ZZ} > 300$ GeV/c^2) the total backgrounds are tiny.

This article presents a search for a diboson resonance in data corresponding to 2.5–2.9 fb^{-1} of integrated luminosity in $\sqrt{s} = 1.96$ TeV $p\bar{p}$ collisions at the CDF II detector at the Fermilab Tevatron, in the decay channel $X \rightarrow ZZ$. These ZZ diboson processes have been well-studied at the LEP experiments, which observed no significant deviation from the standard model expectation up to an e^+e^- center-of-mass energy of 207 GeV [4–7]. The LEP data place only indirect constraints on heavier, resonant ZZ diboson production [8], however, and direct production constraints at high ZZ diboson masses must be probed at hadron colliders. To the previously published CDF search for four-electron production via $X \rightarrow ZZ \rightarrow eeee$ with data corresponding to 1.1 fb^{-1} of integrated luminosity [9], we now add the dijet channels $eejj$ and $\mu\mu jj$, which improve sensitivity at very high X masses where their background is negligible, and the four-electron or muon channels $ee\mu\mu$ and $\mu\mu\mu\mu$, which contribute sensitivity to new physics at intermediate masses where the $Z + $jet($s$) backgrounds are larger.

Because there are four or more outgoing leptons or quarks, the analysis is sensitive to single lepton and jet reconstruction efficiencies to approximately the fourth power. In particular, events may often have one or more leptons with $|\eta| > 1$ where muon acceptance and tracking efficiency are lower than for $|\eta| < 1$. Consequently the four-lepton channels motivate development and use of techniques to improve electron and muon reconstruction and identification efficiencies while exploiting the kinematics of the signature to keep backgrounds low. To augment forward muon coverage, the present analysis also employs, for the first time, a new method of reconstructing charged particles in the silicon detectors using constraints from particle traces in forward regions with partial wire tracker coverage.

The aim of the search is sensitivity to any massive particle that could decay to ZZ. Though we avoid focus on any one specific model, we choose a benchmark process that is implemented in several popular Monte Carlo generation programs, the virtual production of gravitons in a simple Randall-Sundrum RS1 scenario [1,10], to fix acceptance for the search and quantify its sensitivity. The geometry of the model consists of two three-branes separated from each other by a single extra dimension. Boundary conditions at the branes quantize the momentum in the extra dimension, leading to a Kaluza-Klein tower of discrete, massive gravitons. In RS1 scenarios with the standard model particles confined to either brane, a

discovery would involve graviton decays directly to photons or leptons—the graviton branching ratio to ZZ is significant but the Z boson branching ratio to leptons is small. In more complex but well-motivated scenarios with SM particles allowed in the extra dimension, however, graviton decays to photons, leptons, and light jets can be suppressed, and dibosons become an important discovery channel [11,12].

The organization of this article is as follows: Section II describes relevant components of the CDF II detector; Section III, the event selection; Section IV, the background estimates; and Sec. V, the results.

II. THE CDF II DETECTOR

The CDF II detector is a general purpose magnetic spectrometer surrounded by electromagnetic and hadronic calorimeters and muon detectors designed to record Tevatron $p\bar{p}$ collisions. We briefly describe the components of the detector relevant to this search. A complete description can be found elsewhere [13].

A combination of tracking systems reconstructs the trajectories and measures momenta of charged particles in a 1.4 T solenoidal magnetic field. Trajectories of charged particles are reconstructed using an eight-layer silicon microstrip vertex tracker [14] at radii $1.3 < r < 29$ cm from the nominal beam line[1] and a 96-layer open-cell drift chamber (COT) providing eight superlayers of alternating stereo and axial position measurements [15] at large radii $43 < r < 132$ cm. The COT provides full geometric coverage for $|\eta| < 1.0$. The average radius of the lowest radius axial (stereo) COT superlayer is 58 (46) cm, providing partial coverage for $|\eta| < 1.7(1.9)$. The silicon tracker provides full coverage for $|\eta| < 1.8$.

Outside the tracking volume, segmented electromagnetic (EM) lead-scintillator and hadronic (HAD) iron-scintillator sampling calorimeters measure particle energies [16]. The central ($|\eta| < 1.1$) calorimeters are arranged around the interaction point in a projective-tower cylindrical geometry, divided azimuthally into 15° wedges. This calorimeter measures electron energies with a resolution of $[\sigma(E)/E]^2 = (13.5\%)^2/E_T + (2\%)^2$. The forward calorimeters ($1.1 < |\eta| < 3.6$) are arranged in an azimuthally-symmetric disk geometry and measure electron energies with a resolution of $[\sigma(E)/E]^2 = (16.0\%)^2/E + (1\%)^2$. Wire chambers (scintillator strips) embedded in the central (forward) EM calorimeters at $\sim 6X_0$, the average depth of shower maximum, provide

---

[1]CDF uses a cylindrical coordinate system in which θ (ϕ) is the polar (azimuthal) angle, r is the radius from the nominal beam axis, and $+z$ points along the proton beam direction and is zero at the center of the detector. The pseudorapidity is defined as $\eta \equiv -\ln\tan(\theta/2)$. Energy (momentum) transverse to the beam is defined $E_T \equiv E \sin\theta$ ($p_T \equiv p \sin\theta$), where E is energy and p is momentum.

position and lateral shower development measurements for $|\eta| < 2.5$.

Beyond the calorimeters, muon drift chambers and scintillators measure particles that traverse the entire inner and outer detectors and reject the instrumental backgrounds of the central muon triggers. The central muon chambers (CMU) lie just outside the central hadronic calorimeter with ϕ-dependent coverage for $0.03 < |\eta| < 0.63$. The central muon upgrade (CMP) augments the CMU coverage in ϕ and lies behind another approximately 3 interaction lengths of steel. The central muon extension (CMX) extends coverage into the region $0.65 < |\eta| < 1.0$.

The beam luminosity is determined by measuring the inelastic $p\bar{p}$ collision rate with gas Cherenkov detectors [17], located in the region $3.7 < |\eta| < 4.7$.

At each bunch crossing, a three-level trigger system [13] scans the detector output for $|\eta| < 1.1$ electrons or $|\eta| < 1.0$ muons with at least 18 GeV/c of transverse momentum. We accept events that satisfy one of four trigger paths: one that requires a deposition of at least 18 GeV transverse energy in the calorimeter consistent with an electron and a matching COT track with at least 9 GeV/c of transverse momentum; another with fewer electron identification requirements intended to ensure high efficiency for very energetic electrons; a muon path requiring a COT track with at least 18 GeV/c of transverse momentum pointing toward signals in both the CMU and CMP chambers (a CMUP trigger) and traversing the calorimeter consistent with a minimum-ionizing particle; or a similar muon path with signals in the CMX chamber instead of the CMU and CMP chambers.

III. DATA COLLECTION

We use data corresponding to an integrated luminosity of 2.5–2.9 fb^{-1} depending on the data quality criteria applicable to the relevant ZZ diboson decay channel. We separately analyze six channels: $eeee$, $ee\mu\mu$, $\mu\mu ee$, $\mu\mu\mu\mu$, $eejj$, and $\mu\mu jj$. Events are divided into the six categories based on the trigger, where the first lepton denotes the required trigger path, and the presence of lepton and jet candidates identified using the criteria listed in Tables I, II, III, and IV. The trigger lepton criteria are the most stringent; subsequent kinematic signature selections yield very low backgrounds, allowing very efficient identification criteria to be used for the other lepton candidates. Events accepted by either electron trigger path and containing at least one electron candidate that fired the electron trigger and satisfied the offline selection criteria are excluded from the muon-triggered categories. There are no events that satisfy the requirements of more than one category.

During this selection we identify the events containing at least two leptons (including the trigger lepton) using the nominal CDF event reconstruction software. We reprocess these events using a revision of the software with improved

TABLE I. Calorimeter electron identification criteria. We require Had/EM, the ratio of energies measured in the hadronic and electromagnetic calorimeters, to be less than $f(E) = 0.055 + 0.00045 \times (E/\text{GeV})$ where E is the measured calorimeter energy. Iso_{cal} is the calorimeter energy measured within $\Delta R = 0.4$ centered on the electron, excluding the electron energy. η_{det} is calculated assuming an origin at $z = 0$. LshrTrk is a lateral shower shape variable described in Ref. [18].

Criteria	Trigger	Central	Forward
E_T (GeV)	>20	>5	>5
$|\text{Track}z_0|$ (cm)	<60	<60	
Had/EM	$<f(E)$	$<f(E)$	<0.05
$\text{Iso}_{\text{cal}}/E_{\text{cal}}$	<0.2	<0.2	<0.2
$|\eta_{\text{det}}|$			<2.5
LshrTrk	<0.4		
Track p_T (GeV/c)	>10		

tracking, including more efficient forward tracking algorithms, and then select all final particles from the reprocessed data. In this way, we avoid CPU-intensive reconstruction of a 96.6% subset of the sample that has no chance to pass our final selection. Nevertheless, two subsets of the data corresponding to 200 pb^{-1} of integrated luminosity each were fully reprocessed without the initial two-lepton selection and analyzed to confirm that the procedure used for the full dataset is fully efficient for events of interest to the analysis.

The electron criteria listed in Tables I and II are nearly identical to the previous *eeee* analysis [9]. The double Z boson mass peak signature admits little background, allowing appreciably more efficient electron criteria than those used for many other CDF analyses (for example, Ref. [13]). We require either an isolated calorimeter cluster with electronlike energy deposition or, to recover acceptance, an isolated track pointing at uninstrumented regions of the calorimeters. Such regions constitute approximately

TABLE II. Track electron identification criteria. Tracks must consist of measurements in several COT superlayers. Silicon measurements are not required. Iso_{trk} is the scalar sum of the momenta of all tracks measured within a circle of $\Delta R = 0.4$ centered on the electron track direction. ΔR_{EM} is the separation in the $\eta - \phi$ plane between the electron track and the nearest calorimeter electron cluster, as defined in Table I.

Criteria	
p_T (GeV/c)	>10
Axial superlayers	>3
Stereo superlayers	>2
$|\text{Track}z_0|$ (cm)	<60
$p_{\text{trk}}/ (\text{Iso}_{\text{trk}} + p_{\text{trk}})$	>0.9
$|d_0|$	$<\begin{cases} 200\ \mu\text{m} & \text{silicon} \\ 2\ \text{mm} & \text{no silicon} \end{cases}$
ΔR_{EM}	>0.2

17% of the solid angle for $|\eta| < 1.2$ and would otherwise reduce our four-electron acceptance by a factor of 2. The transverse energy threshold for nontrigger electrons is 5 GeV. As the mass of the signal resonance $X \rightarrow ZZ$ increases, the energies of the two Z boson decay products become asymmetric in the detector frame, and thus our criteria must efficiently select leptons with transverse momentum of order 10 GeV/c as well as leptons with p_T of hundreds of GeV/c.

The muon criteria listed in Table III require an isolated track satisfying basic track quality criteria and depositing minimal energy in the calorimeter. We make use of a new track reconstruction algorithm, described in the Appendix, and apply less stringent energy and isolation requirements than typical for CDF high p_T analyses so as to increase our acceptance and efficiency. Muon candidate tracks may be matched to information in the muon chambers, but to recover acceptance lost due to gaps in chamber coverage and to recover efficiency lost due to pointing requirements, chamber matching is not required except for the trigger muon.

Jets must satisfy the criteria listed in Table IV and jet energies are corrected for instrumental effects [20]. Before relying on the jet energy measurements for the two-lepton two-jet analysis, we have verified that these corrections balance transverse momentum in the $Z + \text{jet}(s)$ events considered here. We choose kinematic requirements on individual jet energies, on dijet invariant masses, and on four-body masses involving jets so that the systematic uncertainties on $X \rightarrow ZZ$ signal acceptances and efficiencies from mismodeling of QCD radiation or jet reconstruction effects are small.

Figures 1 and 2 show comparisons of the peaking and background components of the dielectron and dimuon yield. The combination of our changes to the identification criteria and to the tracking algorithms increases the peak yield by factors of 1.8 and 4.3, respectively.

Measurements of the $p\bar{p} \rightarrow \gamma^*/Z \rightarrow ee$ and $p\bar{p} \rightarrow \gamma^*/Z \rightarrow \mu\mu$ cross sections provide an important test of our understanding of the trigger, reconstruction, and identification efficiencies and Monte Carlo modeling for this new lepton selection. We divide the data into 18 data-taking periods and measure each of the above efficiencies for each period. For each period, we then compute the Drell-Yan cross section for all combinations of trigger and lepton type using a signal plus background fit to the data and Drell-Yan Monte Carlo. The average instantaneous luminosity tends to increase with data-taking period as Tevatron upgrades were brought online. Figures 3 and 4 show the resultant cross sections and their dependence on time.

For the cases where both electron energy measurements come from the calorimeters, the fit signal function is a Breit-Wigner fixed to the world average Z boson mass and width convolved with a Gaussian resolution function. In

TABLE III. Muon identification criteria. The CMU, CMP, and CMX match variables compare the track position extrapolated to the relevant muon chambers with the chamber position measurements. The nontrigger p_T requirement is lower for tracks with muon chamber information attached. Iso_{cal} is the sum of calorimeter energies measured in towers within a circle of $\Delta R = 0.4$ centered on the muon tower. E_{EM} and E_{HAD} are the electromagnetic and hadronic calorimeter energies recorded in towers intersected by the muon track, and $f_{EM}(p^{trk}) = 4 + \max(0, 0.0115 * (\frac{p^{trk}}{GeV/c} - 100))$ and $f_{HAD}(p^{trk}) = 12 + \max(0, 0.028 * (\frac{p^{trk}}{GeV/c} - 100))$ are functions of the track momentum. The cuts on track curvature κ, its uncertainty σ_κ, and the χ^2 probability of the fit $Prob(\chi^2, n_{dof})$ reject poorly measured tracks.

Criteria	CMUP	CMX	Nontrigger
$p_T^{trk}(GeV/c)$	>20	>20	>2, 10
CMU match	<10 cm		
CMP match	<20 cm		
CMX match		<10 cm	
	Common to all categories		
Iso^{cal}/p^{trk}	<0.2		
E_{EM} (GeV)	$<f_{EM}(p^{trk})$		
E_{HAD} (GeV)	$<f_{HAD}(p^{trk})$		
κ/σ_κ	>2.5		
$Prob(\chi^2, n_{dof})$	$>10^{-10}$		
$|z_0|$ (cm)	<60		
$|d_0|$	$<\begin{cases} 200\ \mu m & silicon \\ 2\ mm & no\ silicon \end{cases}$		

the trigger plus track lepton sample, where there is a significant radiative tail below the Z boson mass, the signal function is a Crystal Ball function. In the combined sample both functions are included. In all cases, the background function is an exponential. The combined result for the electron selection, 249.4 ± 1.6 pb for the mass range $66 < M_{\ell\ell} < 116$ GeV/c^2, is in agreement with the dedicated CDF measurement $\sigma_{\gamma*/Z} \times Br(p\bar{p} \to \gamma^*/Z \to \ell\ell) = 254.9 \pm 3.3(stat.) \pm 4.6(sys.)$ [13] and is evidence that the constituent efficiencies and scale factors are understood well.

Note that there are large variations in the trigger plus track electron cross section. In these cases, the fit to the data underestimates or overestimates the amount of power-law background contamination of the low dielectron mass radiative tail of the Z boson. The independent fit to the

combination of all selections has a higher signal to noise ratio and is not sensitive to this effect.

The results for the muon selection also show good agreement with the other CDF measurements, except for a 20% shift in the first period and up to a 10% shift in many of the later periods. The discrepancies are due to imperfect modeling of tracking-related muon identification efficiencies for the new reconstruction software. Based on these
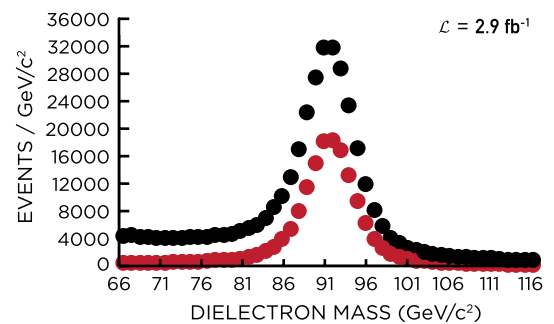

FIG. 1 (color online). $Z \to ee$ yield and background comparison between dielectron candidates consisting of a trigger electron and an electron candidate satisfying either (lower set of points) the CDF standard electron criteria or (upper set of points) the criteria employed in the present analysis. The peak yield increases from about 146 000 with the standard criteria to 256 000 candidates with our optimized criteria. The corresponding increase in continuum background is modest, a factor of 2.0 for 81–101 GeV/c^2. This background is later suppressed by the four-body kinematic selection.
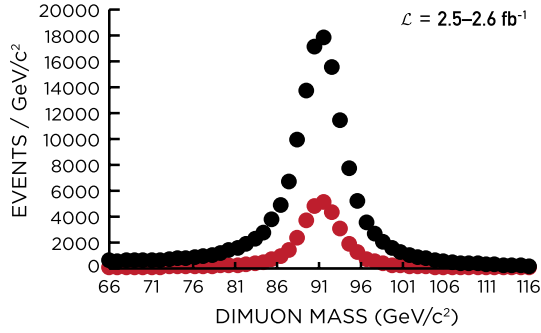
TABLE IV. Jet identification criteria. The JETCLU algorithm is discussed in Ref. [19]. ΔR_{EM} is the separation in the η-ϕ plane between centroids of the jet cluster and the nearest electron cluster.

Selection criteria	
Algorithm	JETCLU 0.4 cone
E_T^{raw} (GeV)	>10
$|\eta_{centroid}|$	<3.64
E_{EM}/E_{tot}	<0.95
ΔR_{EM}	>0.4

FIG. 2 (color online). $Z \to \mu\mu$ yield and background comparison between dimuon candidates consisting of a trigger muon and an muon candidate satisfying either (lower set of points) the CDF standard muon criteria or (upper set of points) the criteria employed in the present analysis. The peak yield increases from about 35 000 candidates with the standard criteria and tracking to 150 000 candidates with our optimized criteria and tracking. The continuum background increases by a factor of 14 for 81–101 GeV/c^2. This background is later suppressed by the four-body kinematic selection.

results, we assign a 20% systematic uncertainty on the signal acceptance for each of the six channels. In part because much of the data were collected with the CMUP trigger and during periods with measured cross sections in good agreement with expectation, and because two of the six analysis channels do not involve muons, this systematic uncertainty over-covers the observed variation in cross section and is the dominant uncertainty for the analysis. Nevertheless, the final sensitivity of the analysis improves substantially on the earlier *eeee* search [9].
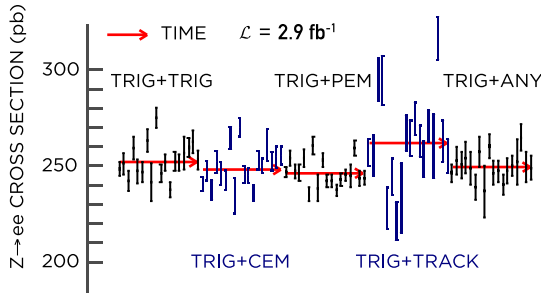
FIG. 3 (color online). $Z \to ee$ cross sections (and averaged cross sections) for $66 < M_{\ell\ell} < 116$ GeV/c^2 and various selections. The horizontal axis indicates the 18 periods for five selections in succession: two trigger electrons (252.1 ± 1.2 pb), a trigger electron and a central calorimeter electron (TRIG + CEM, 248 ± 1.1 pb), a trigger electron and a forward calorimeter electron (TRIG + PEM, 246.2 ± 0.9 pb), a trigger electron and a track electron (TRIG + TRACK, 262.1 ± 2.3 pb), and, calculated separately, the combination of a trigger electron and any electron selected using the analysis criteria (249.4 ± 1.6 pb). The averaged cross sections are indicated by horizontal lines. Uncertainties are statistical only with the correlated luminosity uncertainty not shown.
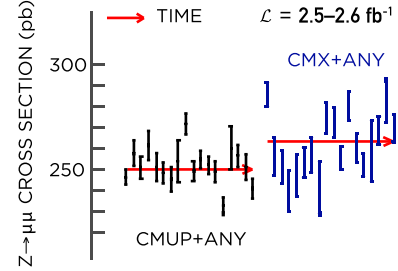

FIG. 4 (color online). $Z \to \mu\mu$ cross sections (and averaged cross sections) for $66 < M_{\ell\ell} < 116$ GeV/c^2 and various selections. The horizontal axis indicates the 18 periods for two selections in succession: a CMUP trigger muon and another muon satisfying the analysis criteria (250.0 ± 1.2 pb) and a CMX trigger muon combined with another selected muon (263.4 ± 1.8 pb). The averaged cross sections are indicated by horizontal lines. Errors are statistical only with the correlated luminosity uncertainty not shown.

IV. KINEMATIC ANALYSIS

After selecting electrons, muons, and jets, we consider all possible four-lepton $\ell\ell\ell\ell$ or two-lepton two-jet $\ell\ell jj$ combinations for each event that contains a trigger lepton. No requirement is made on the mass or charge of dilepton pairs. Any two particles must have a minimum separation $\Delta R = \sqrt{\Delta \eta^2 + \Delta \phi^2}$ of 0.2. Dilepton pairs with tracks present for both leptons must point back to the same z_0 production location in order to suppress background from additional pileup interactions. Track timing information is used for a very pure veto of muon and track electron pairs consistent with cosmic rays. There are no events that appear in more than one ZZ diboson decay channel.

For the four-lepton channels, we consider all possible combinations of leptons for each event and select the one that minimizes a χ^2 variable quantifying consistency between the dilepton masses and the Z boson pole mass:

$$\chi^2_{ZZ} = \sum_{i=1,2} \frac{(M_Z^{(i)} - 91.187 \text{ GeV}/c^2)^2}{\sigma^2_{M^{(i)}} + \sigma^2_{\Gamma}},$$

where $\sigma_{M^{(i)}}$ is the detector mass resolution computed from the individual lepton calorimeter or tracking measurements for the dilepton mass $M_Z^{(i)}$ and a Gaussian approximation with $\sigma_{\Gamma} = 3.25$ GeV/c^2 allows for the nonzero width of the Z boson resonance.

For the $\ell\ell jj$ channels, we consider all possible combinations of leptons and jets. We select the two highest E_T jets and the dilepton pairing that minimizes the first term of the equation above. This explicitly avoids possible Z boson mass bias in the dijet mass spectrum that would complicate the background estimate discussed in the following section. We then require $M_Z > 20$ GeV/c^2 for each pairing and, for the dijet channels, $\chi^2_Z < 25$ for the leptonic Z boson.

A priori we define our signal region to be $M_X > 300$ GeV/c^2 so as to avoid most standard model

backgrounds. For the $\ell\ell\ell\ell$ modes we further require $\chi^2_{ZZ} < 50$ and for the $\ell\ell jj$ modes we require $65 < M_{jj} < 120$ GeV/c^2. Each event may contain additional leptons, jets, or other particles beyond the four that contribute to the signal candidate.

V. BACKGROUND ESTIMATES

For both the four-lepton and the dijet channels, the dominant backgrounds at high M_X are a mixture of $Z +$ jets, $W^{\pm} +$ jets, multijets, and various lower-rate processes resulting in one or more hadrons that mimic an electron or muon. The diboson processes $W^{\pm}Z \to jj\ell\ell$, $ZZ \to \ell\ell\ell\ell$, and $ZZ \to \ell\ell jj$ peak at $\chi^2_{ZZ} < 50$ or $65 < M_{jj} < 120$ GeV/c^2, while all other backgrounds do not peak in both Z boson masses simultaneously. We use a PYTHIA Monte Carlo model [21] with the CDF detector simulation to estimate the small contribution from resonant diboson

processes and fit sideband data to collectively estimate all backgrounds that do not contain two bosons, collectively referred to as nonresonant background.

We estimate the $\ell\ell\ell\ell$ background by extrapolating the yield in the $185 < M_X < 300$ GeV/c^2 region to the signal region ($M_X > 300$ GeV/c^2 and $\chi^2_{ZZ} < 50$) using a shape determined from a sample enhanced in nonresonant background. In order to construct samples enriched in this background, four-lepton candidates are selected in which some of the reconstructed leptons are "antiselected" to fail one or more lepton identification criteria. Antiselected electrons must fail the HAD/EM energy selection and antiselected muons must fail the minimum-ionizing energy selection. To further increase available statistics, the isolation requirement is removed for both categories. Events reconstructed with the standard CDF processing that contain at least one trigger lepton and one antiselected lepton are included in the reprocessing discussed in
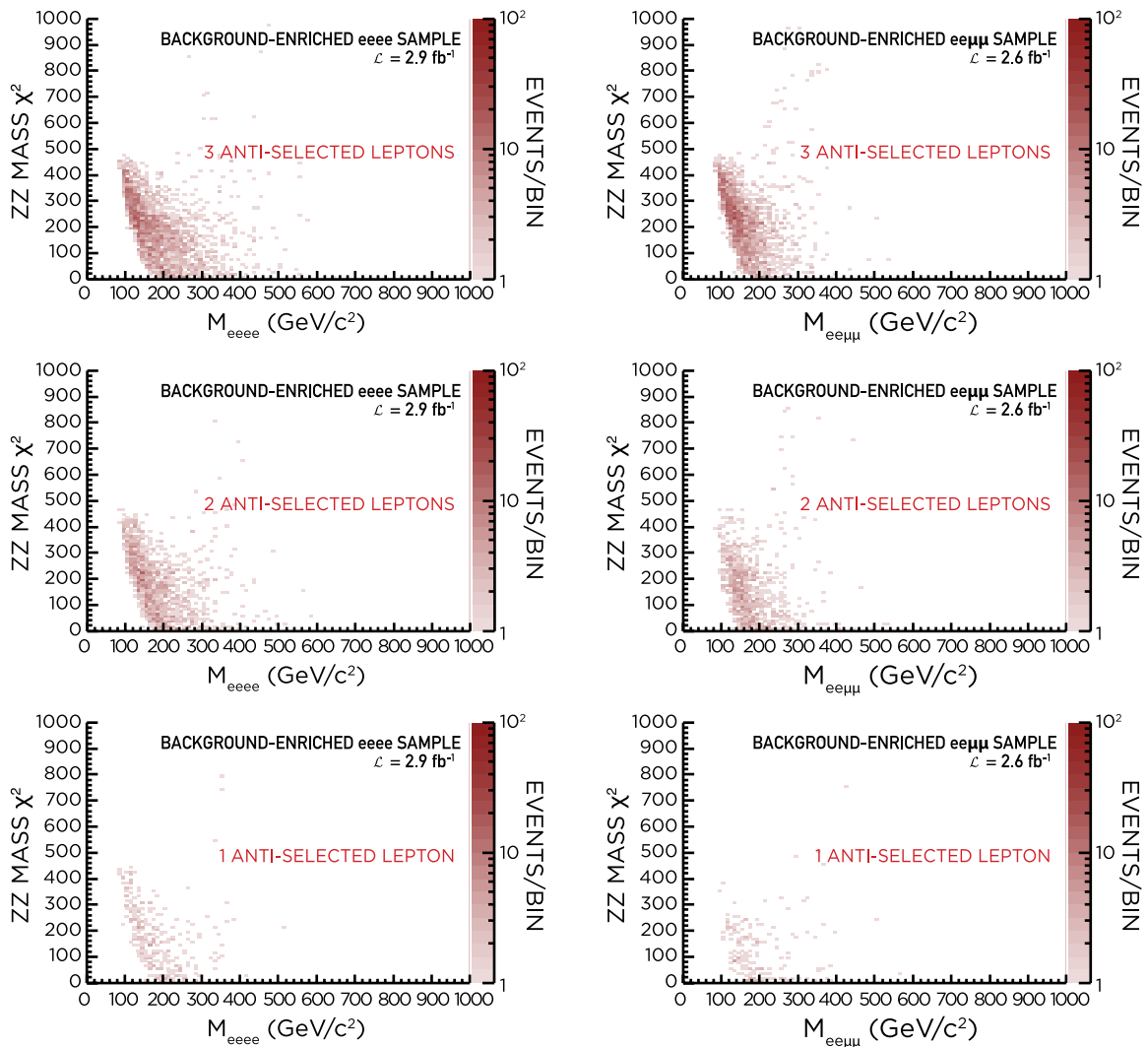

FIG. 5 (color online). χ^2_{ZZ} vs M_X distributions for the four-electron and electron-triggered two-electron two-muon sideband samples with 1, 2, and 3 antiselected leptons.
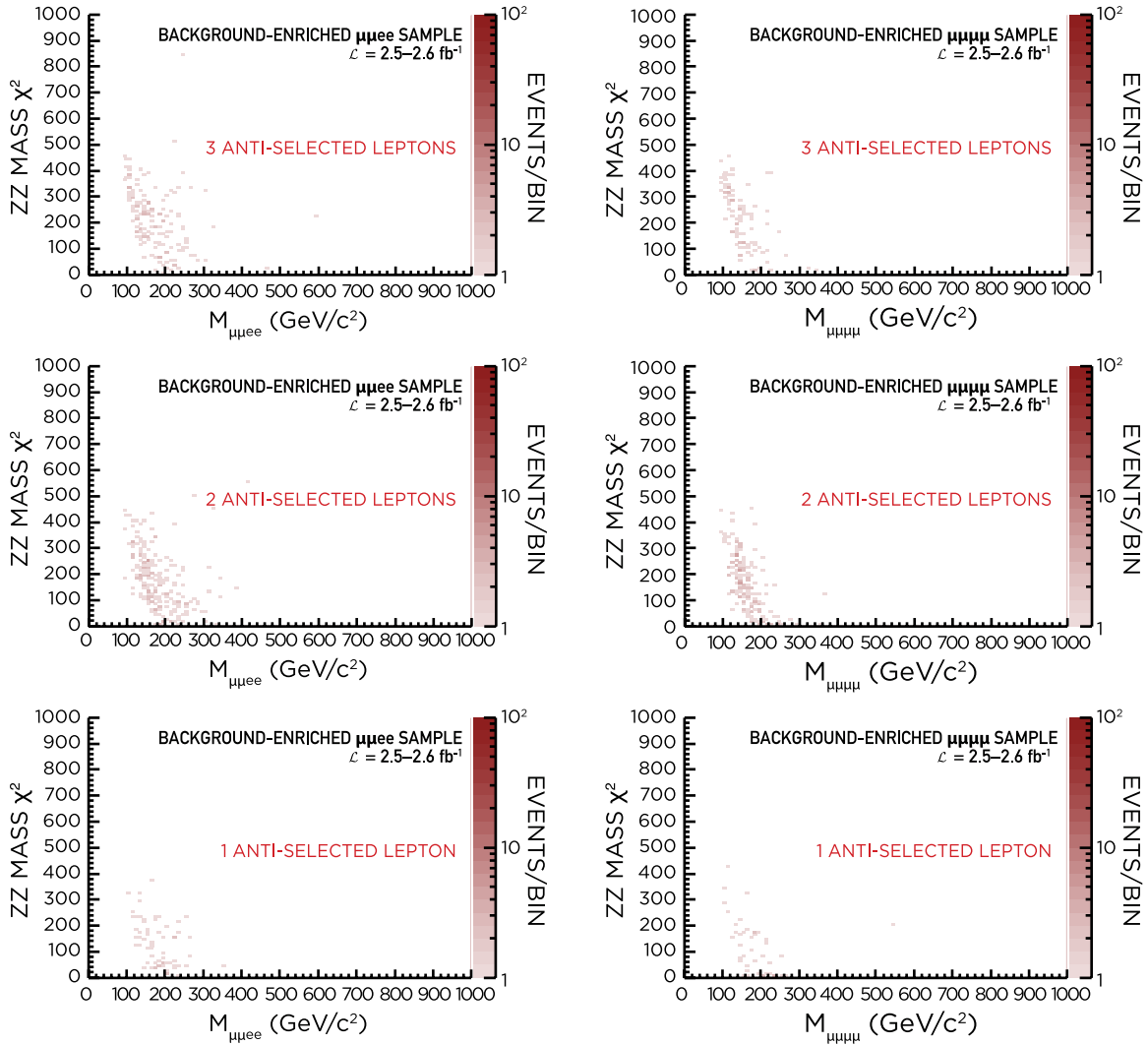
FIG. 6 (color online). χ^2_{ZZ} vs M_X distributions for the muon-triggered two-electron two-muon and four-muon sideband samples with 1, 2, and 3 antiselected leptons.

Sec. III. The χ^2_{ZZ} vs M_X distributions for the resultant samples are shown in Figs. 5 and 6.

Figures 7 and 8 show the invariant mass distributions of trigger lepton plus antiselected lepton pairings for electrons and muons, respectively. The absence of an appreciable peak indicates few resonant Z boson events survive the antiselection.

The two samples of four-body candidates that consist of a trigger lepton and either two- or three-anti-selected leptons with $M_X > 185$ GeV/c^2 and $\chi^2_{ZZ} < 500$ are then fit simultaneously to the empirical form

$$f(\chi^2_{ZZ}, M_X) = M_X^{\gamma} \cdot e^{\tau \chi^2_{ZZ}}$$
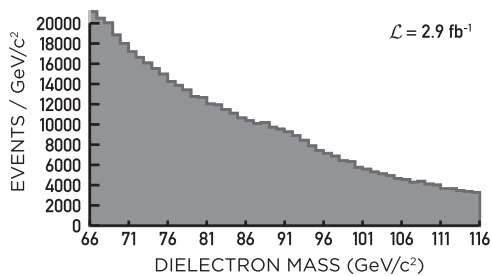
FIG. 7. Invariant mass distribution for pairs of candidates consisting of a trigger electron and an antiselected electron.
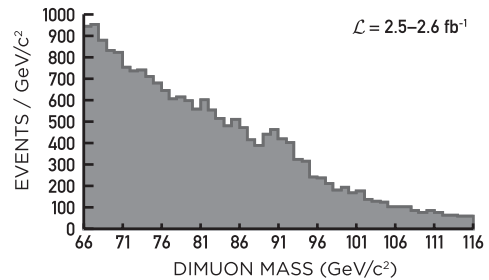

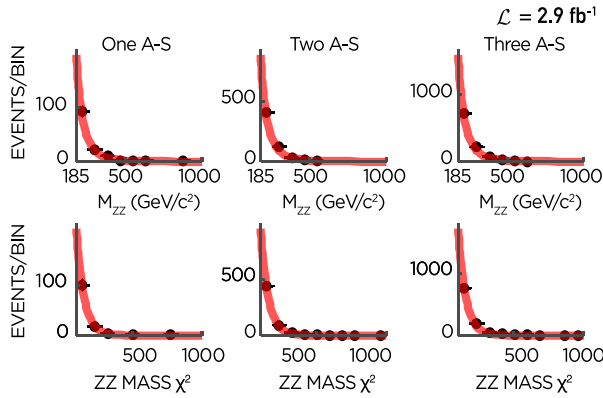FIG. 8. Invariant mass distribution for pairs of candidates consisting of a trigger muon and an antiselected muon.

FIG. 9 (color online). M_{eeee} and χ^2_{ZZ} for the one-, two-, and three-anti-selected (A-S) four-electron samples, and the results of the simultaneous nonresonant background shape fit to the two- and three-anti-selected electron samples.
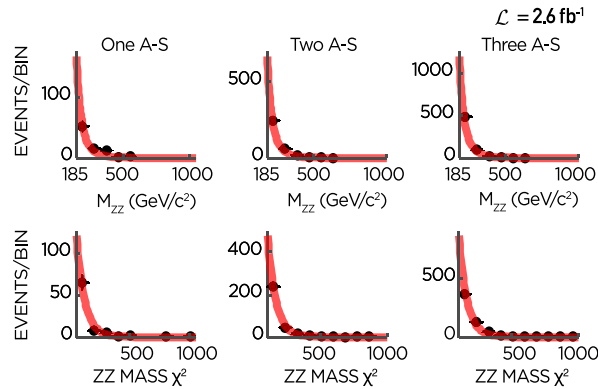

FIG. 10 (color online). $M_{ee\mu\mu}$ and χ^2_{ZZ} for the one-, two-, and three-anti-selected (A-S) lepton samples for the electron-triggered two-electron two-muon channel, and the results of the simultaneous nonresonant background shape fit to the two- and three-anti-selected lepton samples.
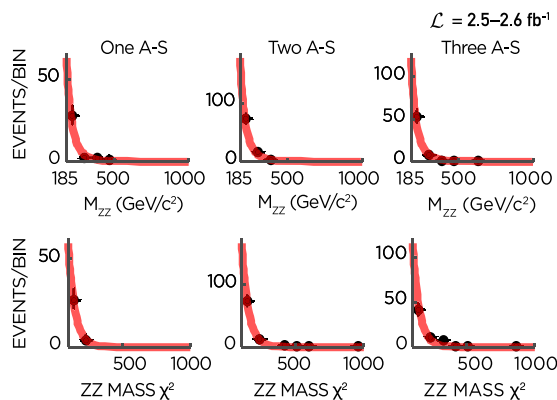

FIG. 11 (color online). $M_{\mu\mu ee}$ and χ^2_{ZZ} for the one-, two-, and three-anti-selected (A-S) lepton samples for the muon-triggered two-electron two-muon channel, and the results of the simultaneous nonresonant background shape fit to the two- and three-anti-selected lepton samples.
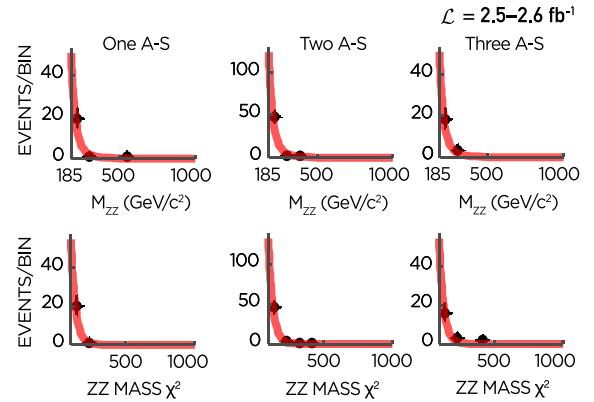

FIG. 12 (color online). $M_{\mu\mu\mu\mu}$ and χ^2_{ZZ} for the one-, two-, and three-anti-selected (A-S) four-muon samples, and the results of the simultaneous nonresonant background shape fit to the two- and three-anti-selected muon samples.

to determine the falling shape of the $M_{\ell\ell\ell\ell}$ distribution (the power-law parameter γ) and the relationship of the number of events in the $\chi^2_{ZZ} < 50$ ZZ window to the number in the off-mass sidebands (the exponential decay parameter τ). As background composition and fake rate kinematic dependence varies with trigger and lepton type, we fit these sidebands separately for the $eeee$, $ee\mu\mu$, $\mu\mu ee$, and $\mu\mu\mu\mu$ background shapes. Figures 9–12 show one-dimensional projections of the fit result for each channel against the fitted two- and three-anti-selected lepton χ^2_{ZZ} and $M_{\ell\ell\ell\ell}$ data as well as the one antiselected sample, which is not used in the fit. Table V lists the fit parameters obtained with their statistical uncertainty.

The background shapes obtained from these fits are normalized so that the sums of the integrals for $185 < M_X < 300$ GeV/c^2 and the simulation-derived diboson predictions match the number of events observed with $185 < M_X < 300$ GeV/c^2 in the four-lepton samples. The shapes are then extrapolated into the low χ^2_{ZZ}, high M_X $\ell\ell\ell\ell$ signal regions. The statistical uncertainty on the normalization is the dominant source of uncertainty for the four-lepton nonresonant background prediction.

As one test of the independence of the nonresonant predictions to the number of selected/antiselected leptons, Tables VI and VII show the parameters and yield predictions obtained by fitting γ for each sample independently of the others. All of the yield predictions for a given signal

TABLE V.   Four-lepton background fit results.

Channel	γ	τ
$eeee$	-4.39 ± 0.09	-0.0184 ± 0.0005
$ee\mu\mu$	-5.4 ± 0.2	-0.0161 ± 0.0005
$\mu\mu ee$	-5.3 ± 0.3	-0.020 ± 0.002
$\mu\mu\mu\mu$	-6.5 ± 0.6	-0.030 ± 0.003

TABLE VI. Comparison of nonresonant background mass shape parameter γ fitted independently in the individual sideband samples with the simultaneous fit to the two- and three-anti-selected lepton samples.

Channel	$eeee$	$ee\mu\mu$
Simultaneous	-4.39 ± 0.09	-5.42 ± 0.15
3 antileptons	-4.22 ± 0.11	-5.19 ± 0.17
2 antileptons	-4.50 ± 0.15	-4.70 ± 0.21
1 antilepton	-4.21 ± 0.30	-3.63 ± 0.32
0 antileptons	-5.04 ± 0.94	-3.54 ± 0.78
Channel	$\mu\mu ee$	$\mu\mu\mu\mu$
Simultaneous	-5.25 ± 0.34	-6.51 ± 0.61
3 antileptons	-4.98 ± 0.50	-6.3 ± 1.1
2 antileptons	-4.96 ± 0.41	-6.60 ± 0.73
1.antileptons	-5.25 ± 0.73	-5.33 ± 0.92
0 antileptons	-5.7 ± 1.6	-4.4 ± 1.3

TABLE VII. Nonresonant background predictions for a characteristic example (the 410–590 GeV/c^2 four-body mass range appropriate for a 500 GeV/c^2 signal) from fits of the individual sideband samples, compared with the prediction from the simultaneous fit to the two- and three-anti-selected lepton samples.

Channel	$eeee$	$ee\mu\mu$
Simultaneous	0.64 ± 0.29	0.128 ± 0.064
3 antileptons	0.65 ± 0.31	0.093 ± 0.048
2 antileptons	0.54 ± 0.26	0.166 ± 0.091
1 antilepton	0.58 ± 0.30	0.40 ± 0.24
0 antileptons	0.51 ± 0.35	0.82 ± 0.59
Channel	$\mu\mu ee$	$\mu\mu\mu\mu$
Simultaneous	0.130 ± 0.077	0.063 ± 0.040
3 antileptons	0.094 ± 0.060	0.058 ± 0.044
2 antileptons	0.127 ± 0.078	0.064 ± 0.043
1 antilepton	0.095 ± 0.065	0.17 ± 0.13
0 antileptons	0.14 ± 0.12	4.2 ± 3.8

mass and decay channel are consistent with each other within the statistical uncertainty.

The sideband data fit for the $\ell\ell jj$ nonresonant background estimates consist of events containing a dilepton pair with $\chi^2_Z < 25$ and a dijet pair with either $40 < M_{jj} < 65$ GeV/c^2 or $120 < M_{jj} < 200$ GeV/c^2. The M_{jj} spectrum near the Z boson pole mass is exponentially falling before imposing any requirement on M_X but linear for events with $M_X > 300$ GeV/c^2, where the effect of the four-body mass cut is to sculpt a peak in the dijet mass at $M_{jj} \gg 200$ GeV/c^2 (see Fig. 13). We linearly interpolate the background expectation for $65 < M_{jj} < 120$ GeV/c^2 from the lower and higher M_{jj} sideband data. To avoid underestimating the background at very high M_X where these sidebands are empty, we model the population of either sideband vs M_X with an exponential fit to the available data to obtain the numbers used in the interpolation. Figure 14 shows the numbers of events in the two dijet
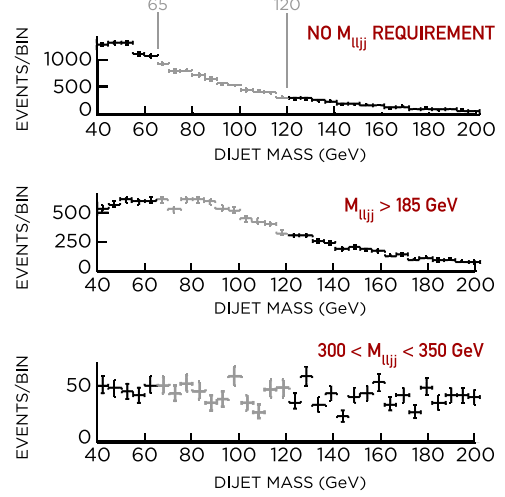

FIG. 13 (color online). Dijet mass spectra for two-electron two-jet candidates with $\chi^2_{ee} < 25$ and three M_{eejj} requirements: no requirement, $M_{eejj} > 185$ GeV/c^2, and $300 < M_{eejj} < 350$ GeV/c^2, beyond which the shape of the dijet mass in the Z boson region is linear.
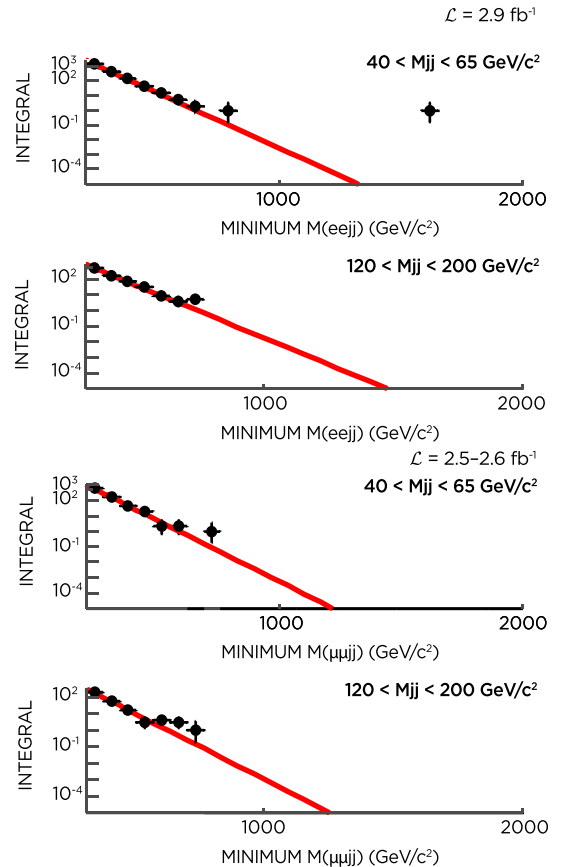

FIG. 14 (color online). Number of two-lepton two-jet events with $40 < M_{jj} < 65$ GeV/c^2 and $120 < M_{jj} < 200$ GeV/c^2 as a function of the minimum M_{lljj} mass requirement, along with the exponential fit to each that is used to interpolate the background prediction for the $65 < M_{jj} < 120$ GeV/c^2 region.

mass sidebands as a function of the requirement on minimum four-body mass and the exponential fits. Exponential functions model the data well.

As one unbiased test of the prediction of the dijet mass spectrum, we repeat the selection and fit procedure on samples consisting of events containing a trigger lepton plus an antiselected lepton and at least two jets. Comparison of the fit predictions against these $65 < M_{jj} < 120$ GeV/c^2 data, which are depleted of signal, show the method performs well (Tables VIII and IX). The disagreement in the lowest M_{eejj} bin for this and other control samples is a result of a slight deviation from an exponential distribution. This residual variation is taken as an extra systematic uncertainty in the lowest mass bin.

We determine the backgrounds resonant in both Z boson masses with Monte Carlo models normalized to the cross sections predicted by MCFM [22]. In the $\ell\ell jj$ channels, our dijet mass resolution and analysis selection does not distinguish between the $W^{\pm}Z \to jj\ell\ell$ and $ZZ \to jj\ell\ell$, and so the background from both processes is present.

Tables X, XI, XII, XIII, XIV, and XV show the total prediction for each analysis channel. At each signal mass,

the predictions are integrated over the four-body mass range listed in Table XVI. The uncertainties listed for the diboson predictions consist of the error on the MCFM cross section ($\approx 7\%$), the uncertainty on the luminosity (6%), and the statistical uncertainty due to finite Monte Carlo

TABLE X.　Total $eeee$ backgrounds with $\chi^2_{ZZ} < 50$ for each signal mass M_X. The uncertainty includes the ZZ diboson production cross section uncertainty, the luminosity uncertainty, the statistical uncertainty from the simulation, and the statistical uncertainty from the nonresonant background fit.

M_X (GeV/c^2)	SM ZZ	Nonresonant
400	0.22 ± 0.02	1.31 ± 0.44
500	0.086 ± 0.009	0.64 ± 0.29
600	0.045 ± 0.005	0.44 ± 0.18
700	0.020 ± 0.003	0.28 ± 0.20
800	0.007 ± 0.001	0.15 ± 0.12
900	0.005 ± 0.001	0.14 ± 0.11
1000	0.0032 ± 0.0001	0.11 ± 0.10

TABLE VIII.　Comparison of dijet mass fit predictions with data for the trigger electron plus antiselected electron and two-jet channel sample. Shown are the uncertainties on the mean prediction due to fit statistics.

M_{eejj} (GeV/c^2)	Prediction	Observed
350–450	1105 ± 29	941
400–600	488 ± 21	540
500–700	95.6 ± 7.2	115
600–800	18.8 ± 2.0	18
650–950	8.31 ± 1.1	8
750–1050	1.64 ± 0.26	3
800–1200	0.73 ± 0.13	2

TABLE XI.　Total $ee\mu\mu$ backgrounds with $\chi^2_{ZZ} < 50$ for each signal mass M_X. The uncertainty includes the ZZ diboson production cross section uncertainty, the luminosity uncertainty, the statistical uncertainty from the simulation, and the statistical uncertainty from the nonresonant background fit.

M_X (GeV/c^2)	SM ZZ	Nonresonant
400	0.19 ± 0.02	0.33 ± 0.13
500	0.067 ± 0.007	0.128 ± 0.064
600	0.035 ± 0.004	0.075 ± 0.047
700	0.014 ± 0.002	0.041 ± 0.029
800	0.004 ± 0.001	0.019 ± 0.013
900	0.003 ± 0.001	0.016 ± 0.013
1000	0.0013 ± 0.0006	0.012 ± 0.011

TABLE IX.　Comparison of dijet mass fit predictions with data for the trigger muon plus antiselected muon and two-jet channel sample. Shown are the uncertainties on the mean prediction due to fit statistics.

$M_{\mu\mu jj}$ (GeV/c^2)	Prediction	Observed
350–450	23.7 ± 4.0	22
400–600	9.4 ± 2.2	9
500–700	1.48 ± 0.59	2
600–800	0.23 ± 0.15	1
650–950	0.093 ± 0.072	1
750–1050	0.015 ± 0.017	0
800–1200	0.0059 ± 0.0084	0

TABLE XII.　Total $\mu\mu ee$ backgrounds with $\chi^2_{ZZ} < 50$ for each signal mass M_X. The uncertainty includes the ZZ diboson production cross section uncertainty, the luminosity uncertainty, the statistical uncertainty from the simulation, and the statistical uncertainty from the nonresonant background fit.

M_X (GeV/c^2)	SM ZZ	Nonresonant
400	0.077 ± 0.008	0.32 ± 0.16
500	0.027 ± 0.003	0.130 ± 0.077
600	0.014 ± 0.002	0.078 ± 0.055
700	0.0065 ± 0.0010	0.044 ± 0.034
800	0.0018 ± 0.0007	0.021 ± 0.017
900	0.0014 ± 0.0006	0.018 ± 0.017
1000	0.0011 ± 0.0005	0.014 ± 0.013

TABLE XIII. Total $\mu\mu\mu\mu$ backgrounds with $\chi^2_{ZZ} < 50$ for each signal mass M_X. The uncertainty includes the ZZ diboson production cross section uncertainty, the luminosity uncertainty, the statistical uncertainty from the simulation, and the statistical uncertainty from the nonresonant background fit.

M_X (GeV/c^2)	SM ZZ	Nonresonant
400	0.090 ± 0.010	0.21 ± 0.11
500	0.036 ± 0.005	0.063 ± 0.040
600	0.018 ± 0.002	0.031 ± 0.023
700	0.0082 ± 0.0015	0.015 ± 0.013
800	0.0018 ± 0.0007	0.0056 ± 0.0049
900	0.00011 ± 0.00005	0.0046 ± 0.0042
1000	0.0009 ± 0.0005	0.0031 ± 0.0030

TABLE XIV. Total $eejj$ backgrounds with $65 < M_{jj} < 120$ GeV/c^2 for each signal mass M_X. The uncertainty includes diboson cross section uncertainties, the uncertainty on the luminosity, the statistical uncertainty from the simulation, and the uncertainties from the nonresonant background fits.

M_X (GeV/c^2)	SM ZZ	SM $W^\pm Z$	Nonresonant
400	5.72 ± 0.97	9.4 ± 1.1	483 ± 18
500	2.43 ± 0.58	3.25 ± 0.46	128.0 ± 8.2
600	0.99 ± 0.36	1.10 ± 0.22	47.4 ± 4.1
700	0.19 ± 0.18	0.60 ± 0.16	14.9 ± 1.7
800	$0^{+0.11}$	0.158 ± 0.083	2.86 ± 0.46
900	$0^{+0.11}$	0.095 ± 0.067	1.75 ± 0.31
1000	$0^{+0.11}$	$0^{+0.067}$	0.77 ± 0.16

TABLE XV. Total $\mu\mu jj$ backgrounds with $65 < M_{jj} < 120$ GeV/c^2 for each signal mass M_X. The uncertainty includes diboson cross section uncertainties, the uncertainty on the luminosity, the statistical uncertainty from the simulation, and the uncertainties from the nonresonant background fits.

M_X (GeV/c^2)	SM ZZ	SM $W^\pm Z$	Nonresonant
400	2.90 ± 0.57	6.04 ± 0.73	162 ± 11
500	1.30 ± 0.38	2.06 ± 0.32	37.7 ± 4.4
600	0.57 ± 0.26	0.73 ± 0.17	12.6 ± 2.0
700	0.26 ± 0.19	0.229 ± 0.93	3.53 ± 0.72
800	0.09 ± 0.13	0.023 ± 0.040	0.57 ± 0.16
900	$0^{+0.10}$	$0^{+0.032}$	0.33 ± 0.10
1000	$0^{+0.10}$	$0^{+0.032}$	0.133 ± 0.045

TABLE XVI. Signal binning used for limit setting.

Signal mass (GeV/c^2)	Bin half width (GeV/c^2)
$400\pm$	70
$500\pm$	90
$600\pm$	130
$700\pm$	160
$800\pm$	160
$900\pm$	230
$1000\pm$	280

the normalization uncertainty due to the small number of events in the $185 < M_X < 300$ GeV/c^2 four-lepton control regions. The nonresonant and diboson background systematic uncertainties are negligible compared to the statistical uncertainty on the total background.

VI. RESULTS

We optimized all selections and estimated all backgrounds before examining the data with $M_{llll} > 300$ GeV/c^2 or with a dilepton pair having $\chi^2_Z < 25$ and a dijet pair with $65 < M_{jj} < 120$ GeV/c^2. Figures 15 and 16 show the data in these regions and the combined resonant and nonresonant background predictions for all four-lepton channels and for both dijet channels. In all cases the data agree with the total background prediction and provide no compelling evidence for resonant ZZ diboson production. The highest-mass $\ell\ell\ell\ell$ event (577 GeV/c^2) consists of four muons. For this event, one Z boson candidate has a mass of 79 ± 4.2 GeV/c^2 and the other Z boson candidate has a mass of 400 ± 170 GeV/c^2. The large mass uncertainty of the second Z boson comes from a large curvature uncertainty in the measurement of one

statistics, which is the dominant uncertainty on the diboson prediction at high four-body mass, though a negligible component of the total background uncertainty. The uncertainties listed for the nonresonant backgrounds consist of the statistical uncertainty from the shape parameters and
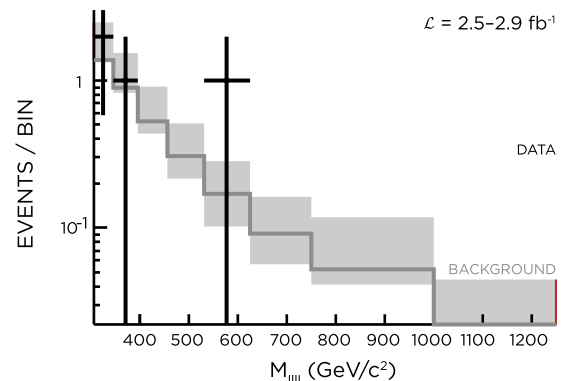

FIG. 15 (color online).   Prediction and data for all four-lepton channels combined. The background prediction for each bin consists of the integral of the nonresonant background functions and diboson Monte Carlo determined in Sec. V. The background predictions agree with the data.
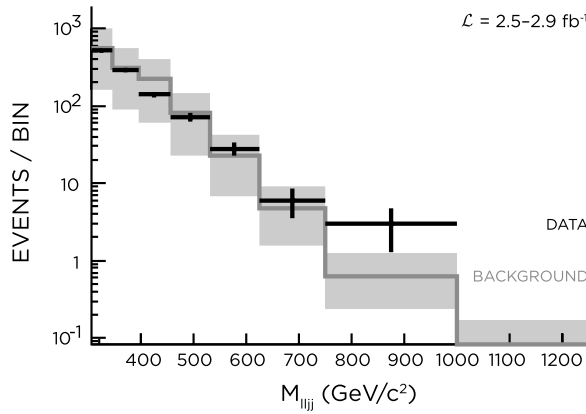
FIG. 16 (color online). Prediction and data for both $\ell\ell jj$ channels combined. The background prediction for each bin consists of the integral of the nonresonant background functions and diboson Monte Carlo determined in Sec. V. The background predictions agree with the data.

$p_T = 290 \text{ GeV}/c$ muon with few COT hits. The highest-mass $\ell\ell jj$ event $(868 \text{ GeV}/c^2)$ has $M_{ee} = 96.5 \pm 1.3 \text{ GeV}/c^2$ and $M_{jj} = 77.8 \pm 6.5 \text{ GeV}/c^2$.

Absent evidence of a signal, we communicate our sensitivity to $X \to ZZ$ processes by setting limits with an acceptance from a widely-available HERWIG Monte Carlo process [23], the spin-2 Kaluza-Klein graviton. The total acceptance times efficiency for this process varies between roughly 40–50% for a given four-lepton channel and between 20–40% for a given dijet channel (Fig. 17). At higher masses, the fraction of Z boson decays increases in which the angular separation between products is too
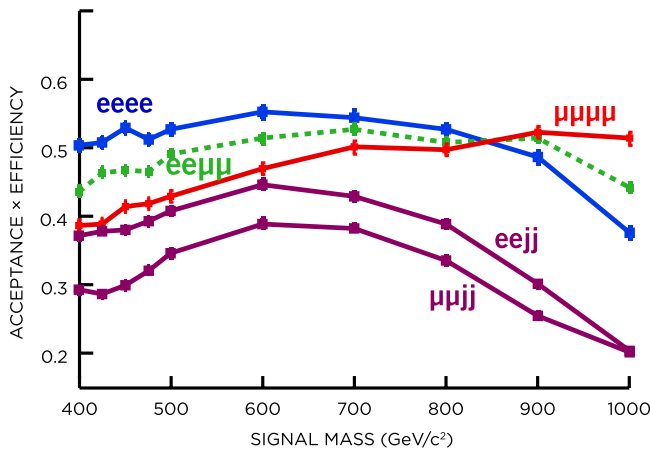
FIG. 17 (color online). Products of acceptance times efficiency for each of the graviton analysis channels and their dependence on graviton mass. These do not include ZZ diboson branching ratios, which for each $ZZ \to \ell\ell jj$ mode are approximately 40 times the branching ratios for $ZZ \to eeee$ or $ZZ \to \mu\mu\mu\mu$. The $ee\mu\mu$ and $\mu\mu ee$ acceptances have been summed.
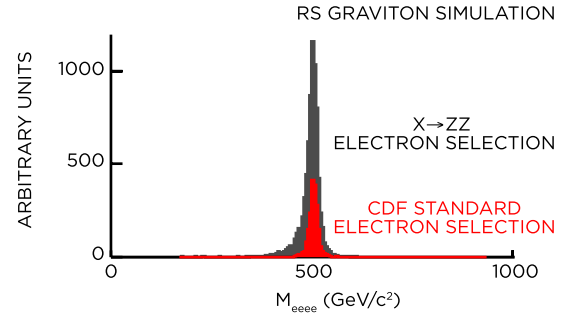

FIG. 18 (color online). Four-electron yield comparison for a 500 GeV/c^2 graviton between (lower histogram) the CDF standard electron selection criteria and (upper histogram) the criteria employed in the present analysis.
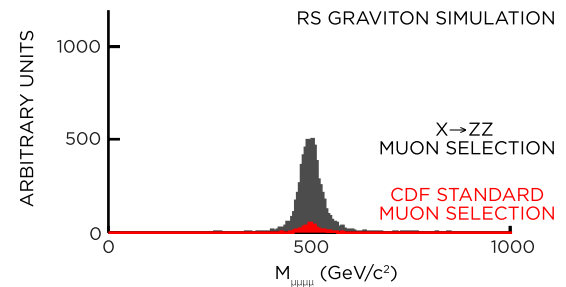

FIG. 19 (color online). Four-muon yield comparison for a 500 GeV/c^2 graviton between (lower histogram) a CDF standard muon selection criteria and (upper histogram) the criteria employed in the present analysis.

small for the calorimeter to resolve. This lowers the acceptances for the dijet modes and, to a lesser extent, the electron modes.

The combined effect of the lepton reconstruction and identification improvements on graviton signal is demonstrated in Figs. 18 and 19 for the four-electron and four-muon channels. We compute data yields and estimates of signal and background by integrating the Monte Carlo predictions and fitted nonresonant background shapes over a set of overlapping, variable-width bins for signal masses from 400 GeV/c^2 to 1 TeV/c^2 (Table XVI). Each signal bin width is chosen to be large enough to fully contain the four-body mass distribution expected for an intrinsically narrow signal and the broadening from systematic effects. Table XVII shows the total background prediction and observed data yields in each of these bins.

We calculate 95% credibility upper limits as a function of signal mass using a six-channel product of Bayesian likelihoods and a uniform prior for the (non-negative) $X \to ZZ$ cross section. We use marginalized truncated-Gaussian nuisance parameters for the luminosity, background predictions, and signal efficiencies, and we account for systematic uncertainties correlated amongst the six

TABLE XVII. Total background prediction and observed data yields for each of the limit-setting bins in Table XVI. Successive bins are partially correlated. The uncertainty (quoted as the least two significant figures in parentheses) is the systematic uncertainty on the mean background prediction and does not include statistical fluctuation about the mean.

Channel		M_X (GeV/c^2)						
		400	500	600	700	800	900	1000
$eeee$	Expected	1.53(44)	0.73(29)	0.49(18)	0.30(20)	0.16(12)	0.15(11)	0.11(10)
	Observed	0	0	0	0	0	0	0
$ee\mu\mu$	Expected	0.52(13)	0.195(64)	0.110(47)	0.055(29)	0.023(13)	0.019(13)	0.013(11)
	Observed	2	0	0	0	0	0	0
$\mu\mu ee$	Expected	0.397(16)	0.157(77)	0.092(55)	0.050(34)	0.023(17)	0.019(17)	0.015(13)
	Observed	0	0	0	0	0	0	0
$\mu\mu\mu\mu$	Expected	0.30(11)	0.099(40)	0.049(23)	0.023(13)	0.0074(49)	0.0047(42)	0.0040(30)
	Observed	1	1	1	1	0	0	0
$eejj$	Expected	498(18)	133.7(82)	49.5(41)	15.7(17)	3.02(48)	1.84(34)	0.77(21)
	Observed	456	142	69	28	7	5	2
$\mu\mu jj$	Expected	171(11)	41.1(44)	13.9(20)	4.02(75)	0.68(21)	0.33(14)	0.13(11)
	Observed	143	41	19	4	2	2	1

channels when appropriate. As discussed earlier, we assign a 20% uncorrelated uncertainty to the total acceptance × efficiency for each channel to account for the observed time-dependent variation in the Drell-Yan $\mu\mu$ cross section, conservatively covering the sum of individual systematic uncertainties such as signal acceptance uncertainties in order to simplify the combination. Studies of the individual uncertainties indicate the largest contribution after the uncertainty due to the $Z \rightarrow \mu\mu$ cross section variation is the 5.9% uncertainty on the luminosity. In addition to the observed limit, we compute expected limits from 10 000 pseudoexperiments at each candidate X mass. Figure 20 shows the resultant limits along with the $k/M_{\text{Pl}} = 0.1$ Randall-Sundrum (RS1) graviton cross section from HERWIG. The present search improves the $\mathcal{O}(4 \text{ pb})$ limit of the earlier $eeee$ search [9] by an order of magnitude.
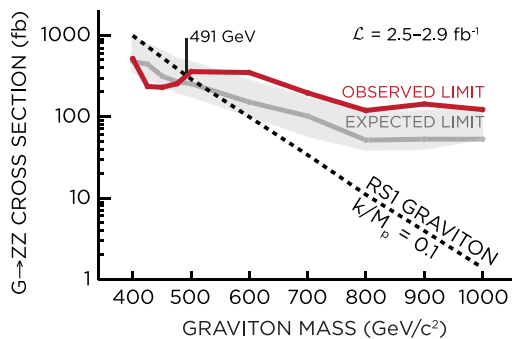

FIG. 20 (color online). 95%-credibility cross section upper limit assuming acceptance for a massive graviton along with the limit and 68% variation expected for the background-only hypothesis.

VII. CONCLUSIONS

We have reported on an improved search for a massive resonance decaying to ZZ dibosons via the $eeee$, $ee\mu\mu$, $\mu\mu\mu\mu$, $eejj$, and $\mu\mu jj$ channels. We find that the four-body invariant mass spectrum above 300 GeV/c^2 is consistent with background estimates derived from sideband data samples and electroweak Monte Carlo models. To quantify our sensitivity, we set limits using the acceptance for a Randall-Sundrum graviton model that are 7–20 times stronger than the previously published direct limits on resonant ZZ diboson production.

APPENDIX

The standard CDF reconstruction software uses two main approaches to reconstruct tracks. High quality central tracking ($|\eta| < 1$) starts in the COT and assembles piecewise segments of up to 12 hits in each superlayer, fits them, and groups them into tracks to which any available silicon hits are then attached in an outside-in search. Afterward, "silicon standalone" tracking starts with all possible combinations of three unused silicon hits, searches the remaining silicon layers, and projects successful tracks into the COT to attach any compatible hits in order to improve the track momentum resolution and lower the fake rate.

The combination of these approaches results in low efficiency in the $1 < |\eta| < 2$ region. Tracks originating from $z = 0$ with $|\eta| < 1.7$ will leave traces of their passage in the lowest-radii superlayers of the COT. Though very

efficient when full COT coverage is available, for $|\eta| > 1$ the central tracking algorithms lose efficiency nearly linearly with $|\eta|$ reaching zero efficiency at about $|\eta| = 1.6$. The silicon fully covers $|\eta| < 1.8$ to compensate for the falling COT efficiency, but the existing silicon-driven tracking algorithms reconstruct tracks with low efficiency and produce low-quality or spurious tracks with poor pointing resolution into the COT. Thus the COT information for forward tracks is rarely exploited.

This analysis employs a thorough revision of the forward and central tracking algorithms in order to reconstruct tracks with better efficiency and resolution, including a new "Backward" algorithm that makes full use of the partial COT coverage. The Backward algorithm, illustrated in Fig. 21 for a simple case, starts by searching the COT for hits unused by the central COT algorithm and constructing segments in one of the inner axial superlayers consisting of no more than 12 hits. At this stage, the position measurements contain a drift sign ambiguity and important drift time corrections, such as large time of flight and sense wire signal propagation times, are unknown and cannot be approximated by the constant corrections assumed for the central segment pattern recognition. The Backward algorithm solves this problem with a variant of the central segment pattern recognition that resolves the drift sign ambiguity and drift time corrections during the search and is optimized for tracking in the low radius, high hit density inner superlayers and near the COT end plates. Once unused COT hit segments are found consistent with a forward track, the algorithm then fits the segments with a beam line constraint to obtain five-parameter helices that intersect the z position of the highest sum p_T z vertex identified using central algorithm tracks. In most
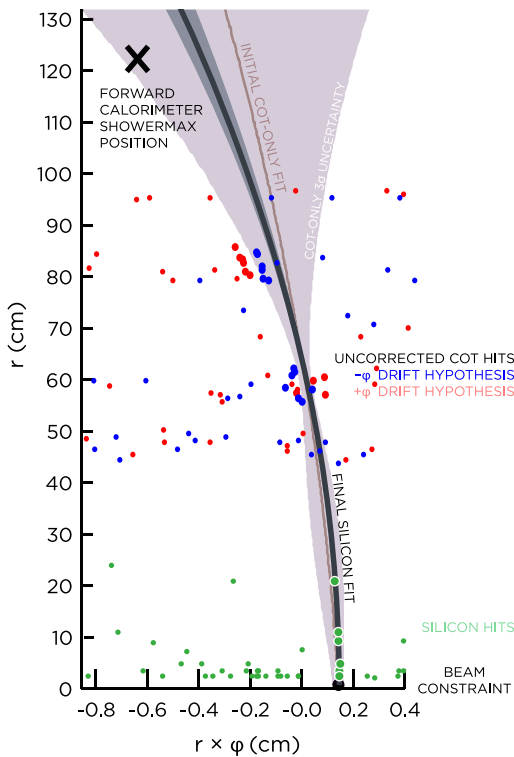

FIG. 21 (color online). A simple example of the Backward tracking algorithm in low luminosity data. In a stretched and rotated $r - \phi$ view of the relevant section of the tracking volume, COT pulses in a single 12-layer axial superlayer indicating two possible hit locations corresponding to $-\phi$ and $+\phi$ drift are processed to identify trajectory segments and fitted to obtain drift time corrections and an initial trajectory with large uncertainties. An iterative Kalman filter search through possible η values for silicon charge clusters consistent with the initial trajectory produces a tree of track possibilities, from which the single best candidate, shown with a projection of the final 3σ uncertainties, is chosen. Also shown is an independent measurement from the forward calorimeter shower maximum scintillator.
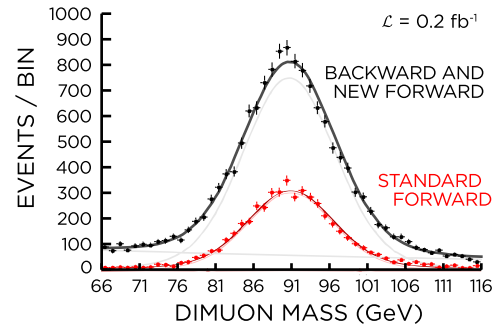

FIG. 22 (color online). $Z \rightarrow \mu\mu$ yield and background comparison in 0.2 fb^{-1} of data for candidates combining a trigger muon with another muon reconstructed by any dedicated forward tracking algorithm for (lower curve) the standard CDF reconstruction and (upper curve) the reconstruction used for the present analysis. The gray curves indicate the shapes and normalization of the signal (Breit-Wigner distribution convolved with a Gaussian resolution function) and background (exponential distribution) components used in the fit. In both cases, attached COT hits and the muon identification criteria listed in Table III are applied.

cases, the fits do not conclusively identify stereo COT measurements in the innermost stereo superlayer, and so multiple helices are obtained corresponding to trajectories through each possible combination of silicon module and polar angle. Drift time corrections are recomputed for each case.

After obtaining initial helix fits, including estimates of the helix uncertainties and correlations obtained from the small number of COT hits, the algorithm begins an outside-in silicon hit search that uses a Kalman filter to correct for energy loss and multiple scattering in the tracker material. After each search completes, quality criteria based on hit pattern, multiple usage, charge deposition, and module operational status are applied to the successful hypotheses, and all surviving hypotheses except those with the most hits are discarded. Finally, the COT is searched for any remaining information, including stereo measurements in inner superlayers.

The Backward algorithm has been validated on a variety of samples, with emphasis on large samples of $Z \to ee$ and $Z \to \mu\mu$ simulation and data. Figure 22 shows the improvement in $Z \to \mu\mu$ yield in muon-triggered data involving higher-quality forward tracks with COT hits in a subset of the data, demonstrating the increase in muon acceptance due to the new software. The lower curve represents the dimuon mass spectrum for the combination of a trigger muon tracked with the central algorithm and a forward muon tracked in the combination of the COT and the silicon detectors with the silicon-driven algorithm in the standard software. The upper curve shows the same spectrum in the new software, where the Backward algorithm has largely superseded the other silicon-driven algorithm. With a modest increase in background, the peak yield has improved by about 260%, corresponding to an approximately 10% increase in the total $Z \to \mu\mu$ yield over the entire detector. The distributions of all forward muon identification variables are qualitatively the same as those of muons found with the central COT-driven algorithm, indicating that we have selected a sample of forward muons with purity comparable to the central muons.

[1] L. Randall and R. Sundrum, Phys. Rev. Lett. **83,** 4690 (1999).

[2] T. Aaltonen *et al.* (CDF Collaboration), Phys. Rev. Lett. **100,** 201801 (2008).

[3] V. M. Abazov *et al.* (D0 Collaboration), Phys. Rev. Lett. **101,** 171803 (2008).

[4] ALEPH Collaboration, Phys. Lett. B **469,** 287 (1999).

[5] DELPHI Collaboration, Eur. Phys. J. C **30,** 447 (2003).

[6] L3 Collaboration, Phys. Lett. B **572,** 133 (2003).

[7] OPAL Collaboration, Eur. Phys. J. C **32,** 303 (2003).

[8] H. Davoudiasl, J. L. Hewett, and T. G. Rizzo, Phys. Rev. Lett. **84,** 2080 (2000).

[9] T. Aaltonen *et al.* (CDF Collaboration), Phys. Rev. D **78,** 12008 (2008).

[10] L. Randall and R. Sundrum, Phys. Rev. Lett. **83,** 3370 (1999).

[11] K. Agashe, H. Davoudiasl, G. Perez, and A. Soni, Phys. Rev. D **76,** 36006 (2007).

[12] L. Fitzpatrick, J. Kaplan, L. Randall, and L.-T. Wang, J. High Energy Phys. 09 (2007) 013.

[13] A. Abulencia *et al.* (CDF Collaboration), J. Phys. G **34,** 2457 (2007).

[14] A. Sill *et al.*, Nucl. Instrum. Methods Phys. Res., Sect. A **447,** 1 (2000).

[15] T. Affolder *et al.*, Nucl. Instrum. Methods Phys. Res., Sect. A **526,** 249 (2004).

[16] L. Balka *et al.*, Nucl. Instrum. Methods Phys. Res., Sect. A **267,** 272 (1988).

[17] D. Acosta *et al.*, Nucl. Instrum. Methods Phys. Res., Sect. A **461,** 540 (2001).

[18] F. Abe *et al.* (CDF Collaboration), Phys. Rev. D **44,** 29 (1991).

[19] F. Abe *et al.* (CDF Collaboration), Phys. Rev. D **45,** 1448 (1992).

[20] A. Bhatti *et al.*, Nucl. Instrum. Methods Phys. Res., Sect. A **566,** 375 (2006).

[21] T. Sjostrand *et al.*, Comput. Phys. Commun. **135,** 238 (2001).

[22] J. M. Campbell and R. K. Ellis, Phys. Rev. D **60,** 113006 (1999).

[23] G. Corcella *et al.*, J. High Energy Phys. 01 (2001) 010.